RESEARCH ARTICLE

Cost-Effective Vat Orange 3-Derived Organic Cathodes for Electrochemical Energy Storage

Ling Chen,[a] Fangfang Xing,[a] Qiting Lin,[a] Ahsan Waqas,[a] Xiujuan Wang,[a] Thomas Baumgartner,*[b] Xiaoming He*[a]

[a] L. Chen, F. Xing, Q. Lin, A. Waqas, Dr. X. Wang, Prof. Dr. X. He
Key Laboratory of Applied Surface and Colloid Chemistry (Ministry of Education), School of Chemistry and Chemical Engineering
Shaanxi Normal University
Xi'an 710119, P.R. China
E-mail: xmhe@snnu.edu.cn

[b] Prof. Dr. T. Baumgartner
Department of Chemistry
York University
Toronto, ON M3J 1P3, Canada
E-mail: tbaumgar@yorku.ca

Supporting information for this article is given via a link at the end of the document.

Abstract: Organic compounds are desirable alternatives for sustainable lithium-ion battery electrodes. Vat orange 3 (**VO3**, 4,10-dibromoanthanthrone) is a highly cost-effective organic dye containing two conjugated carbonyl groups, that can reversibly accept two electrons. The skeleton also contains two bromine atoms, which allows easy incorporation of the anthanthrone unit into polymers through simple reactions. In this work, we report the preparation of organic cathodes derived from the low-cost **VO3** dye for lithium-organic batteries (LOBs). The results show that polymeric **VO3**-based materials exhibit remarkably high cyclability and rate performance, because of their effective suppression of dissolution. In particular, the sulfide polymer **PATS** shows an initial large-current (0.2 A g^{-1}) discharge capacity of 133 mAh g^{-1} at a potential near 2.4 V. The capacity reaches a maximum capacity of 147 mAh g^{-1} after 24 cycles and is maintained at 132 mAh g^{-1} after 300 cycles. Moreover, a full battery cell with the structure: **PATS** cathode || graphite anode, further delivers an impressive electrochemical performance with an energy density up to 237 Wh kg^{-1} along with an output voltage of 2.3 V. The present study initiates the use of **VO3**-based organics, which show promising potential for future application in LOBs on a large scale.

Introduction

Since the commercialization of Sony Corporation's lithium ion batteries (LIBs) in 1991, LIBs have been dominating the market of portable rechargeable batteries and electric vehicles, due to their high energy density and efficiency.[1-2] Current commercial LIBs feature inorganic transition-metal oxides such as $LiCoO_2$, $LiMn_2O_4$, $LiFePO_4$ or $LiNi_xMn_yCo_zO_2$, which are mainly produced from ores instead of renewable resources. The limited availability of some of the mineral resources and ever-increasing cost have forced researchers to evaluate alternative electroactive materials for batteries. Organic electrode materials are attractive in view of their potentially sustainable production and low carbon footprint.[3-7] One promising advantage of organic materials is their simple structure optimization toward tuning their (in)solubility and electronic conductivity. The past two decades have witnessed an ever-growing interest in pursuing novel, redox-active organic molecules and polymer-based electrodes. A diverse number of structural motifs, such as organic free-radicals,[8-11] phenothiazine,[12-15] dihydrophenazine,[16-17] benzothiadiazole,[18] dibenzothiophenesulfone,[19] azobenzenes,[20-21] viologens,[22-26] and flavin (vitamin B2)[27] have been explored as organic electrodes for batteries. Recently, we developed a class of bio-derived carbonyl-N-methylpyridinium species for high-performance lithium-organic batteries (LOBs).[28-29] However, their practical application is generally hampered by their high cost, undesirable solubility, and complicated synthesis.

Organic carbonyl compounds, such as imides and quinones, are highly promising electrode materials for electrochemical energy storage.[30-35] They can transfer and store at least two electrons during the charge/discharge process. Although they possess adjustable structures with a wide variety of derivatives that can be applied to various metal-ion batteries,[36-39] a major challenge for carbonyl-based organic electrode materials is the unwanted dissolution of the active material in liquid electrolytes, leading to poor rate performance and cycling stability. Many attempts to modify small molecules have been made over the past several decades to address the above issue. By extending the π-skeleton of molecular organic carbonyl compounds or polymerization, their solubility in the electrolyte can be effectively reduced, thereby improving the battery performance.[40-47] Many recent literature examples reveal that different linkers in polymers also significantly affect the conductivity and electrochemistry.[40-47] On the other hand, the relatively high cost of the starting materials and the requirement of multiple synthetic steps, give rise to difficulties for mass production, and restrict real commercial applications. Consequently, rational structure design plays a critical role in improving the performance of quinones.

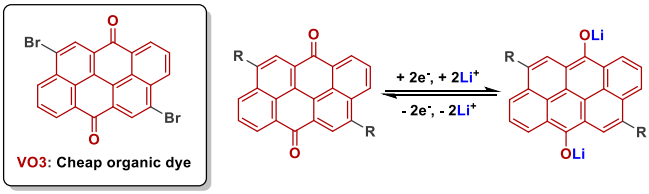

Scheme 1. Structure of **VO3** (left) and proposed reversible Li-ion insertion/de-insertion (right).

Vat orange 3 (**VO3**, 4,10-dibromoanthanthrone, Scheme 1) is a highly cost-effective dye (ca. $30/kg) that is historically known as colorant for fabrics. Its large and flat π surface reduces the solubility in common organic solvents. It contains two conjugated carbonyl groups, that can reversibly accept two electrons. Upon reduction, the generated enolates can be stabilized by large, conjugated structures, making it possible for Li ions to be (de)inserted reversibly at the oxygen atoms. The theoretical specific capacity of anthanthrone is 175 mAh g^{-1}, which is higher than commercial inorganic cathode materials, such as inorganic $LiCoO_2$ (140 mAh g^{-1}). In addition, the presence of bromine atoms at the 4- and 10-positions allows versatile chemical reactivity to further tune the conductivity and solubility.[48] Given the satisfactory theoretical specific capacity and low-cost, **VO3**-derived organics are very promising cathodes for LOBs.

Herein, we report and compare several anthanthrone-based organics (Figure 1a), including two small molecules **VO3** and **AT-Ph**, two conjugated polymers (**PATS** and **PAT-Ph**), as well as their electrochemical energy-storage application. Two different linkers (phenyl vs. sulfur) have been selected for polymer design. Compared to the small molecules **VO3** and **AT-Ph**, the two polymers present remarkably improved cyclability and rate performance, because of their effective suppression of dissolution. Impressively, the sulfide polymer **PATS** exhibits the highest lithium-ion diffusivity, smallest charge-transport resistance, as well as best battery performance. At a current density of 0.2 A g^{-1}, **PATS** shows an initial discharge capacity of 133 mAh g^{-1} at potential range near 2.4 V. The capacity is further increased after 24 cycles to reach a maximum capacity of 147 mAh g^{-1} and is maintained at 132 mAh g^{-1} after 300 cycles. Further increasing mass-loading (up to 5.0 mg cm^{-2}) and high-polymer-content (up to 80 wt%), **PATS** still exhibits decent battery performance,

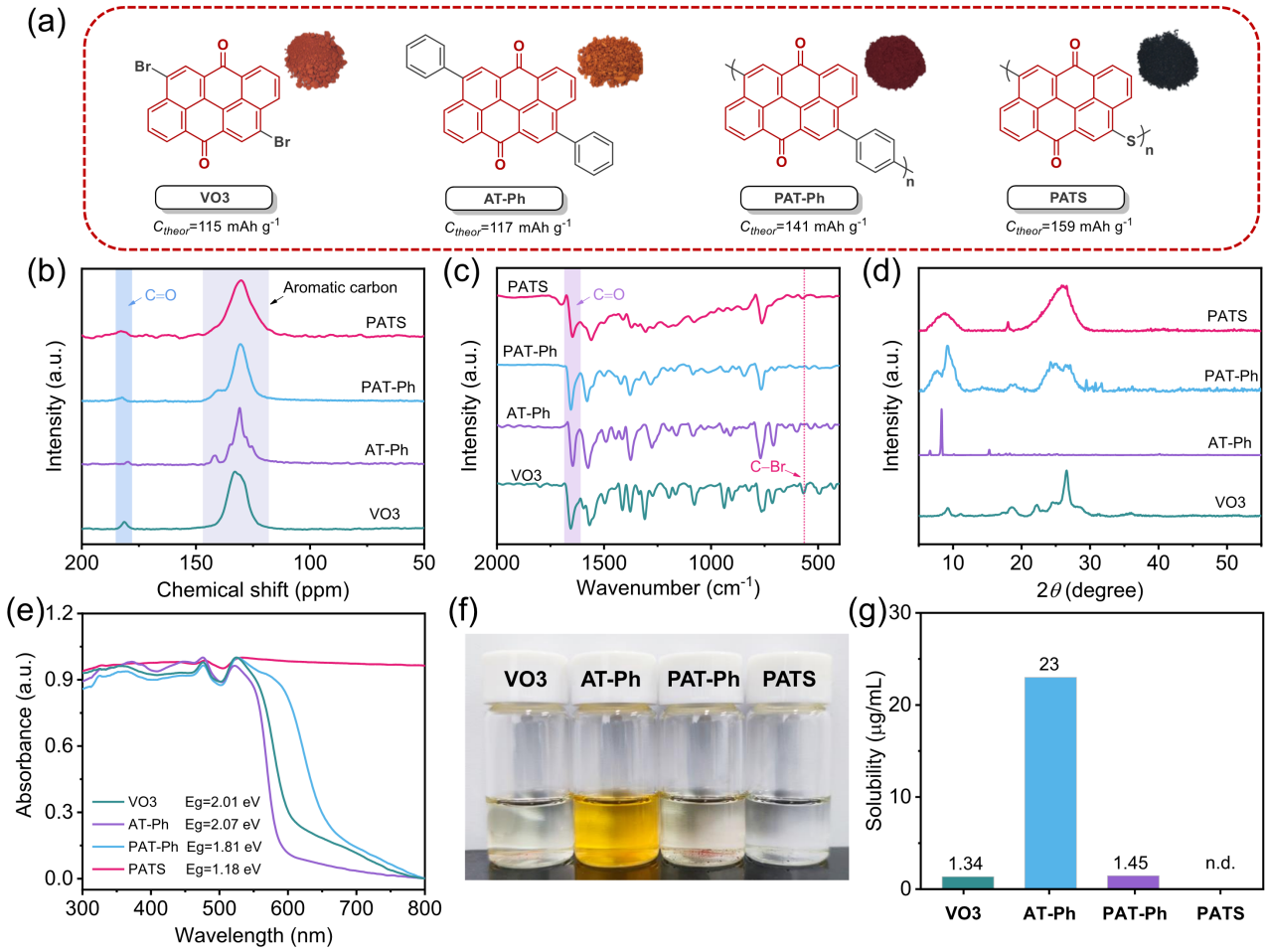

Figure 1. Structures and characterization of **VO3**, **AT-Ph**, **PAT-Ph** and **PATS**. (a) Chemical structures and their color as solids, (b) solid-state ^{13}C NMR spectra, (c) FT-IR spectra, (d) PXRD spectra, (e) UV–Vis diffuse reflectance spectra of the solids, (f) digital photographs of four materials soaked in G4 electrolyte for 3 days, (g) solubility in G4 electrolyte.

demonstrating its potential for large-scale applications. In particular, a full battery with a structure: **PATS** cathode || graphite anode delivers an energy density of 237 Wh kg^{-1} at a current density of 0.1 A g^{-1}, with output voltage of 2.3 V. These results reveal both a high capacity and an excellent cycling stability that are comparable (or even superior to) many transition-metal-oxide-based materials currently being employed. This work highlights the considerable versatility of redox-active anthanthrone materials for the construction of high-performance battery electrodes.

Results and Discussion

Synthesis and Characterization

The synthetic routes to our target species are presented in Scheme S1. The poly(anthanthrone sulfide) (**PATS**) was synthesized by a simple polycondensation of **VO3** and Na_2S in N-methyl pyrrolidone (NMP), according to modified procedure developed by Phillips et al.;[49] the obtained product is black. The 4,10-diphenyl substituted anthanthrone (**Ph-AT**) was prepared by Suzuki coupling of **VO3** with phenylboronic acid in a yield of 87 %.[50-51] Polymer **PAT-Ph** was synthesized in a similar way as **Ph-AT** by using the bifunctional 1,4-phenylenebisboronic acid instead. Notably, all synthetic processes are simple, scalable, and merely use inexpensive chemical feedstocks.

The chemical identities of the products were verified by solid-state ^{13}C nuclear magnetic resonance (^{13}C NMR) and Fourier-Transform Infrared (FT-IR) spectroscopies. As observed from the ^{13}C NMR spectra (Figure 1b), signals in the range of 120-150 ppm correspond to the aromatic carbon atoms, whereas the signals at 180 ppm support the existence of carbonyl entities. The relatively good solubility of **AT-Ph** allowed us to also characterize it by solution ^{1}H NMR (Figure S1). The FT-IR spectra of the two polymers show the characteristic peaks of the C=O functionality at 1647 cm^{-1}, which is nearly identical to that in the small molecules (Figure 1c). This means that the carbonyl groups are well maintained in the polymer structures, and consistent with the ^{13}C NMR results. In addition, the band at 569 cm^{-1} assigned to C-Br stretching of **VO3**, is absent in **AT-Ph** and **PAT-Ph** and significantly attenuated in **PATS**, which is a good indication of the successful synthesis of the target products. The two small molecules (**VO3** and **AT-Ph**) are highly crystalline, as revealed by their sharp peaks in the powder X-ray diffraction (PXRD) spectrum (Figure 1d). By contrast, broad and intense peaks that were observed in the range of 22° to 29° for the two polymers, indicate their semi-crystalline nature and some amount of π–π stacking. Scanning electron microscope (SEM) images (Figure S2) reveal distinct morphologies for **VO3** (short rod, length between 0.1-2 mm), **AT-Ph** (long rods, length > 5 mm), **PAT-Ph** (aggregated nanoparticles with diameters of 0.2-1 mm), and **PATS** (large bulk morphologies). All materials display impressive thermal stability, with a decomposition temperature (T_d) above 300 °C, except **PAT-Ph** with a modest T_d value of 200 °C under nitrogen atmosphere (Figure S3).

The C–S stretching vibrations, typically in the range of 900-1400 cm^{-1}, were not clearly observed for **PATS**, probably due to some spectral overlap. Alternatively, the formation of thioether bond (C–S–C) was nonetheless confirmed by X-ray photoelectron spectroscopy (XPS). The full survey XPS curve of **PATS** confirmed the presence of O, C and S atoms, as well as the absence of Br atoms, lending further support to the efficiency of the polymerization process (Figure S4a). The high-resolution C1s XPS spectrum (Figure S4b), exhibits three clear peaks that can be assigned to C=O (288.7 eV), C–S (286.2 eV) and C=C/C–H (284.6 eV) bonds, respectively. For the high-resolution O1s XPS spectrum (Figure S4c), the two obvious peaks around 533.4 and 531.9 eV are attributed to C–O and C=O bonds, respectively. The high-resolution S2p XPS spectrum reveals two peaks around 164.6 and 163.4 eV that are ascribed to S2p1/2 and S2p3/2, respectively (Figure S4d). The degree of polymerization (n) for **PATS** was estimated to n = 3, based on the results of elemental analysis (see the details in Table S1).

The different substituents (Br vs. phenyl) in the small molecules and the linkers (S vs. phenylene) in the polymers have a pronounced effect on the photophysical properties and solubilities of the four species. The solids of **VO3**, **AT-Ph**, **PAT-Ph** and **PATS** present as orange, yellow, deep red, and black powders, respectively. Figure 1e shows their UV–vis diffuse reflectance spectra in the solid state. **VO3** and **AT-Ph** show broad absorptions between 300–550 nm, with the absorption edge extended to approximately 600 nm. Extending the conjugated backbone in the polymeric species, either via phenylene in **PAT-Ph** or sulfide in **PATS**, leads to a wider absorption in the visible window between 300–600 nm. In particular, **PATS** absorbs all the visible light from 300–800 nm, indicating highly beneficial electronic delocalization along the conjugated backbone; this is consistent with its black color and also indicates high electronic conductivity (*vide infra*). Their optical bandgaps (E_g) calculated from Tauc plots (Figure S5) are 2.01 eV (**VO3**), 2.07 eV (**AT-Ph**), 1.81 eV (**PAT-Ph**) and 1.08 eV (**PATS**), respectively.

The materials' solubility was determined by UV spectrophotometry via soaking the compounds in G4 (tetraglyme) electrolyte for three days and subsequent dilution before measurement (Figure S6). As shown in Figure 1f, only the **AT-Ph** solution displays an obvious yellow color. **AT-Ph** has relatively high solubility of 23 μg mL^{-1}, while the solubilities of **VO3** and **PAT-Ph** are only 1.34 and 1.45 μg mL^{-1}, respectively, and no detectable solubility was observed for **PATS** (Figure 1g). The greatly decreased solubility for two polymers in particular, results from the strong intermolecular *π–π* stacking, which would be beneficial for improving their cycling performance in batteries.

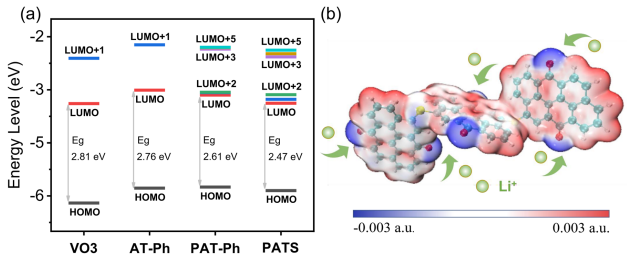

Figure 2. (a) Frontier orbital energy levels of **VO3**, **AT-Ph**, **PAT-Ph** and **PATS** obtained by DFT calculations. (b) Molecular electrostatic potential (MESP) map of **PATS**.

Theoretical Calculations

To obtain a better understanding of the photophysical and electronic properties, density functional theory (DFT) calculations were performed at the B3LYP/6-31G(d) level of theory. For computational convenience, trimers of each polymer were used as model molecules. The calculated energy levels for the small molecules and polymers are summarized in Figure 2a, and their frontier molecular orbital diagrams are shown in Figures S7-S9. In general, the energy level of the lowest unoccupied molecular orbital (LUMO) of an n-type electroactive material is a useful parameter for estimating its relative redox behavior. The characteristics of the LUMOs for all compounds are essentially the same and mainly located on the anthanthrone moieties. For the small molecules, the calculations suggest that two electrons will successively fill the LUMO and LUMO+1 orbitals. Their relatively large gap (*ca.* 1.28 eV) would lead to two separate redox pairs and two distinct flat discharge curves (*vide infra*). In comparison, each trimeric 'polymer model' has two sets of degenerate orbitals; their close energy levels are expected lead to broad redox peaks and sloping discharge curves.

The calculated energy gaps between the highest occupied molecular orbitals (HOMOs) and the LUMOs are in agreement with the trends observed by solid-state UV-vis spectroscopy, but are systematically overestimated by 0.7-0.8 eV for **VO3**, **AT-Ph** and **PAT-Ph**, and 1.3 eV for **PATS**. The likely reason for this observation is that the calculation does not consider the aggregation of the materials, which normally lowers the energy gaps. The largest overestimated values for **PATS** indicate that its intermolecular π–π stacking is the strongest in the series, which is greatly beneficial for improved intralayer conductivity and the total electron-transfer efficiency.

The molecular electrostatic potential (MESP) method was employed to identify the electrophilic and nucleophilic reaction-active sites. On the van der Waals surface of the molecules (Figure 2b and Figure S10), the blue region stands for the negative MESP value (electrophilic center) and the red region represents the positive MESP value (nucleophilic center). Obviously, the four compounds have efficient active sites for charge storge, which are mainly located around C=O groups.

Electrochemical Properties and Half Battery Performance

To investigate the electrochemical performance, we assembled LOBs in coin-type cells with designed materials as the cathode, lithium metal as anode, and 2.0 M lithium bis-trifluoromethanesulfonimide (LiTFSI) in G4 as electrolyte. We first tested electrodes consisting of 60 wt % active materials **(VO3, AT-Ph, PAT-Ph** or **PATS**), 30 wt % multi-wall carbon nanotubes (MWCNTs) and 10 wt % poly(vinylidene fluoride) (PVDF), with mass loading of *ca.* 0.6 mg cm^{-2}. Figure 3a shows the CV profiles of the **VO3-, AT-Ph-, PAT-Ph-** and **PATS**-based electrodes at a scan rate of 0.2 mV s^{-1} with an operating voltage between 1.5 and 3.5 V (vs Li/Li^+). **VO3** shows two pairs of redox peaks with $E_{1/2}$ centered at 2.42 and 2.66 V and a peak separation of 0.36–0.43 V. Two pairs of redox peaks are also observed for **AT-Ph** ($E_{1/2}$ = 2.40 and 2.52 V) and **PAT-Ph** ($E_{1/2}$ = 2.40 and 2.56 V). The reduction/oxidation peaks were negatively shifted, indicating their stronger electron-accepting character, compared to that of **VO3**. Of note, the CV of **PATS** is quite different, where three redox pairs ($E_{1/2}$ = 2.21, 2.44 and 2.67 V) are observed, probably due to an intra-molecular charge transfer from sulfur to anthanthrone. Compared with the voltammograms of the two small-molecule species, the polymers display relatively broad CV profiles that are consistent with the theoretical calculations. Notably, when a wider operating voltage 1.5–4.0 V (vs Li/Li^+) was applied, an additional redox pair at 3.54 V was observed for **VO3**, which was attributed to the irreversible reduction of the C–Br bonds (Figure S11). Such peak was not observed for **AT-Ph**, further providing indirect evidence for the former.

The galvanostatic charge–discharge (GCD) profiles of the four battery electrodes at 0.2 A g^{-1} are presented in Figures 3b and S12. Evidently, two distinct platforms at 2.5/2.3 V and 2.4/2.3 V are observed for the discharging curves of **VO3** and **AT-Ph**, respectively. This observation is in line with the CV data, further verifying the presence of two redox processes. For the polymers, the GCD curves have a relative slope in a potential range of 2.0–2.6 V. These results are highly consistent with the CV data and may be the result of electronic communication along the conjugated backbone that leads to many consecutive reduction processes with small voltage gaps between them. This phenomenon has been also observed for other conjugated carbonyl compounds with two-electron reduction features.[33, 52]

The cycling stabilities of the four materials in LOB devices were verified at a constant current density of 0.2 A g^{-1} between 1.5 and 3.5 V (Figure 3c). The discharge capacity of the **PATS**-based cathode in the second cycle was 133 mAh g^{-1}, after which the capacity gradually increased due to an activation process, reaching a maximum capacity of 147 mAh g^{-1} after 24 cycles; the capacity was stabilized without significant attenuation in the subsequent cycles, and was maintained at 132 mAh g^{-1} after 300 cycles. A similar cycling phenomenon was observed for **PAT-Ph**; where the initial and maximal discharge capacities were 104 and 113 mAh g^{-1}, respectively. The occurrence of "activation processes" was attributed to insufficient contact between the polymer and the electrolyte, which is only gradually improved during the charge/discharge processes, akin to a conditioning process (*vide infra*). In contrast, no activation processes were observed for the small molecule species. **VO3** and **AT-Ph** underwent continuous capacity decay, as a result of undesirable solubility. After 300 cycles, the capacity of **VO3** and **AT-Ph** was measured to only be 40 and 11 mAh g^{-1}, corresponding to 42 % and 10 % of their initial values, respectively. Overall, the different cycling performances of the four materials agrees well their different dissolution behavior, thus leading us to believe that unfavorable dissolution (and not chemical decomposition of the materials) is the dominating factor in capacity fading for the small molecules. Surprisingly, the Coulombic efficiencies are close to 100 % in all cases, verifying the materials' high reversible redox stability.

Next, the rate performance of the four electrodes at various current rates from 0.2 to 2.0 A g^{-1} (after 10 cycles activation at 0.1 A g^{-1}) was explored. As shown in Figure 3d, **PATS** delivered the best capacity, followed by **PAT-Ph**, then **VO3**, and finally **AT-Ph**. The trend is consistent with their varying solubilities. At a low current density of 0.2 A g^{-1}, **PATS**, **PAT-Ph**, **VO3**, and **AT-Ph** exhibited stable capacities of 149, 103, 51 and 47 mAh g^{-1}, respectively. The conjugated polymer backbones in **PATS** and **PAT-Ph** allowed for an ultra-high-rate capability. Increasing the current density did not bring about dramatic drop in capacity. Even at a high current density of 2.0 A g^{-1}, **PATS** and **PAT-Ph** still

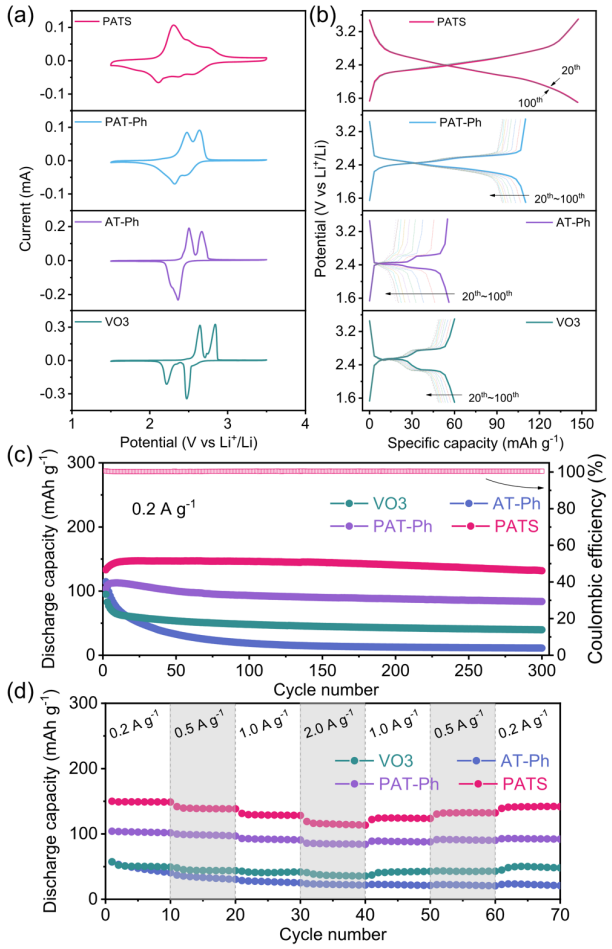

Figure 3. Electrochemistry and battery performance of **VO3**, **AT-Ph**, **PAT-Ph** and **PATS** electrodes in corresponding half-cells with a loading of 6:3:1 active material/MWCNTs/PVDF (mass loading of active materials is about 0.6 mg cm^{-2}). (a) CV of electrodes in a battery configuration at 0.2 mV s^{-1}, (b) galvanostatic charge-discharge profiles at 0.2 A g^{-1}, (c) cycling performance 0.2 A g^{-1}, (d) rate performance at different current densities.

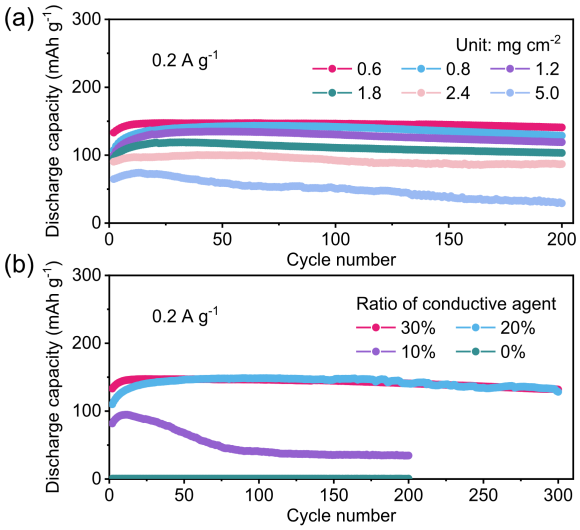

Figure 4. Cycling performance of **PATS** at 0.2 A g^{-1} with (a) different mass-loading from 0.6 to 5.0 mg cm^{-2}, and (b) different content of conductive MWCNTs from 30 % to 0 %.

maintain capacities of 115 and 85 mAh g^{-1}, corresponding to 77 % and 82 % of the initial values, respectively. Importantly, when the current density is shifted back from 2.0 to 0.2 A g^{-1}, nearly quantitative recovery of the initial capacities is observed in all cases, demonstrating their superior stability.

We also measured the performance of **PATS** cathode at higher mass-loading, in order to demonstrate its potential for large-scale applications. As shown in Figure 4a, a progressive capacity loss was observed upon gradually increasing the mass-loading from 0.6–5.0 mg cm^{-2}. This can be attributed to electrode thickness with increasing ion-diffusion distance, leading to the underutilization of active material. After 200 cycles, relatively stable capacities of 141, 128, 119, 103, 87, and 39 mAh g^{-1} can still be maintained with mass-loadings of 0.6, 0.8, 1.2 1.8, 2.4, and 5.0 mg cm^{-2}, respectively. The maximum capacity (74 mAh g^{-1}) of a thick electrode (5.0 mg cm^{-2}) is about 50 % of that of the highest capacity (147 mAh g^{-1}) of a thin electrode (0.6 mg cm^{-2}). Nevertheless, increasing the mass-loading did not show negative effect of cycling stabilities.

Encouraged by these results, we varied the content of conductive additives in the **PATS** electrodes. Typically, a high amount (30–60 wt %) of conductive additive is needed to enhance the electronic conductivity of the electrode. However, the conductive additives do not directly contribute to the charge-storage capacity of the electrodes, and therefore, minimizing the content of conductive additives is desirable to increase the charge-storage capacity. To this end, we fabricated coin-type LOBs by decreasing the content of conductive MWCNTs from 30 % to 0 %, and investigate the cycling performance. As shown in Figure 4b, 20 wt% of MWCNTs as conductive additive is enough for the **PATS** electrode to show satisfactory battery performance. Its specific capacity and cycling performance (128 mAh g^{-1} after 300 cycles) are comparable to that with 30 wt % conductive additives. A superior battery performance with such high polymer content (70 wt %) is unusual, indicating the excellent electronic conductivity of **PATS** as a result of the intramolecular charge transfer from sulfur to the anthanthrone units. However, further reducing the amount of MWCNTs led to dramatic capacity loss; the capacity value with 10 wt% additive only reached 35 mAh g^{-1} after 200 cycles. The specific capacity of pure polymer electrodes (additive free) was zero during cycling.

Mechanism

To better understand the Li$^+$-storage behavior, the electrochemical kinetics were investigated using the CV method reported by Dunn et al.[53] Figures 5a and S13-15 show the CV profiles of the electrodes using **PATS** and the other three species, respectively, at various scan rates from 0.2 to 1.0 mV s^{-1} with 1.5–3.5 V. Multiple redox signals were continuously observed at various scan rates. With elevated scan rates, the cathodic peaks shift to lower potentials, while the anodic peaks shift to higher potentials, which we ascribe to the enhanced polarization. The dependence of the peak current on the scan rate follows the power law that is represented by equation 1:

$$i = av^b \qquad (1)$$

where *i* represents the current of the CV profile, *v* is the sweep rate, and *a* and *b* are adjustable parameters. It has been suggested that the charge storage process is mainly dependent on the *b* value, which is determined by the slope of the log(*i*) versus log(*v*). If *b* equals 0.5, the process can be controlled by semi-infinite linear diffusion, while if *b* has a value of 1, the process is capacitive (surface-controlled).[54] As seen from Figures 5b and S13-15, the *b* values of peaks 1–4 for the two polymers are in the range of 0.8–1.0, which are higher than those of the two small-molecule materials (0.5–0.8), indicating that the charge storage is a fast, surface-controlled process with the polymers. The higher capacitive contributions of the two conjugated polymers indicate efficient insertion and extraction of Li^+ ions, which is favorable for fast charge storage.[55] More accurately, the contribution of capacitive and diffusion-controlled behaviors to the total charge storage can be evaluated as follows (equation 2):[56]

$$i = k_1 v + k_2 v^{1/2} \qquad (2)$$

where $k_1 v$ and $k_2 v^{1/2}$ represent the current contributions from the surface capacitive effects and the diffusion-controlled process, respectively. Figures 5c and S16 depict the capacitive contribution of the **PATS** electrode at different scan rates. The calculated contribution of **PATS** is 90.8 % at 0.6 mV s^{-1}. This result indicates that the electrochemical behavior of **PATS** is mainly dominated by the kinetically fast capacitive process that accounts for its excellent rate performance.[57-58]

In order to further understand the best performance of **PATS**, electrochemical impedance spectroscopy (EIS) was performed to analyze the electrochemical behavior of the four electrodes. The equivalent circuit and Nyquist plots are presented in Figures 5d and 5e. **PATS**-based composite electrodes showed a significantly smaller charge-transport resistance (R_{ct}, denoted by the diameter of the semicircle in high- and intermediate-frequency region) of 71.3 Ω, compared to **PAT-Ph** (94.0 Ω), **AT-Ph** (106.1 Ω), and **VO3** (123.9 Ω). This indicates higher conductivity in **PATS** that results from efficient delocalization of sulfur lone pair to the conjugated polymer backbone. The ion diffusion abilities were further investigated with EIS. According to equation 3, the linear relationship between the real part of impedance (Z') and the reciprocal of the square root of angular frequency ($\omega^{-1/2}$) is quantitatively analyzed to obtain the ion diffusion resistance σ_w, also known as Warburg coefficient.

$$Z' = R_s + R_{ct} + \sigma_w \omega^{-1/2} \qquad (3)$$

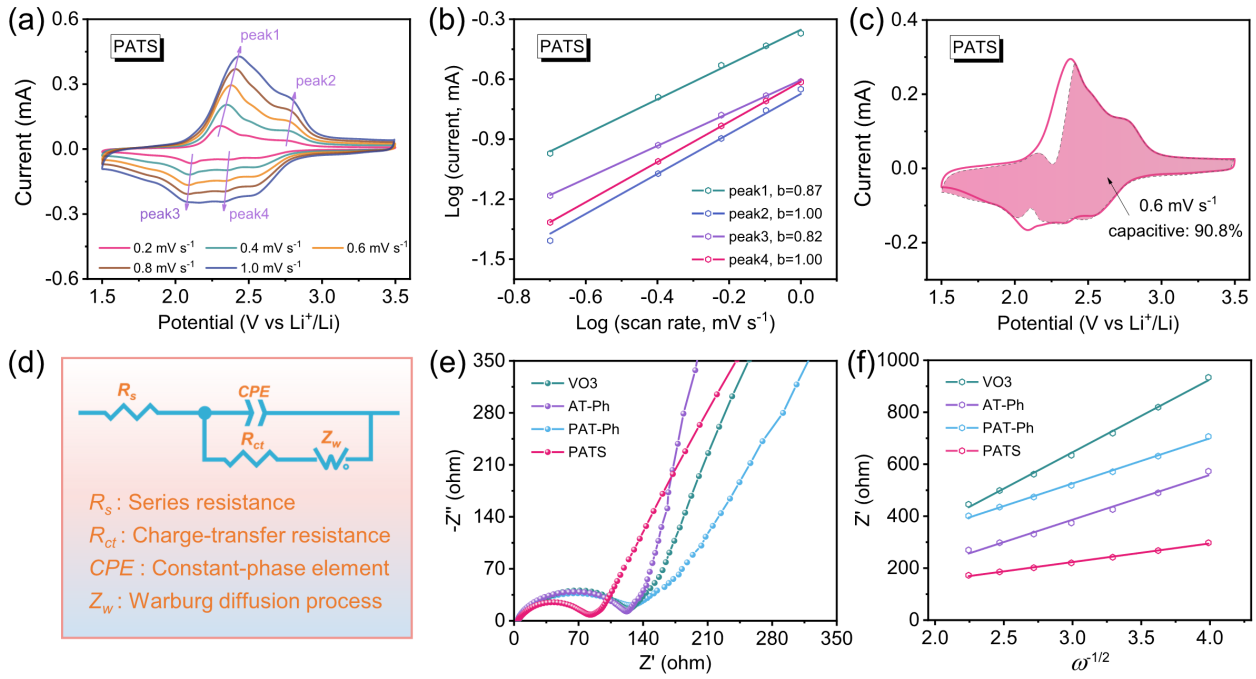

Figure 5. Electrochemical kinetics study. (a) CV of **PATS** at different scan rates, (b) log *i* versus log *v* plots of **PATS** to determine the *b* values of different peaks, (c) capacitive contributions **PATS** to CV curve at 0.6 mV s^{-1}, (d) equivalent circuit used for fitting the experimental data, (e) Nyquist plots of **VO3**, **AT-Ph**, **PAT-Ph**, and **PATS** electrodes before cycling, (f) relationship between the real part of impedance versus low-frequency region.

Table 1. Summary of simulation parameters from the EIS measurements.

	VO3	AT-Ph	PAT-Ph	PATS
R_{ct} (Ω)	123.9	106.1	94.0	71.3
R_s (Ω)	4.6	4.0	3.8	4.2
σ_w (Ω $S^{-1/2}$)	280.0	172.3	173.8	71.7
D_{Li^+} (cm^2 s^{-1})	1.36×10^{-14}	3.60×10^{-14}	3.53×10^{-14}	2.07×10^{-13}

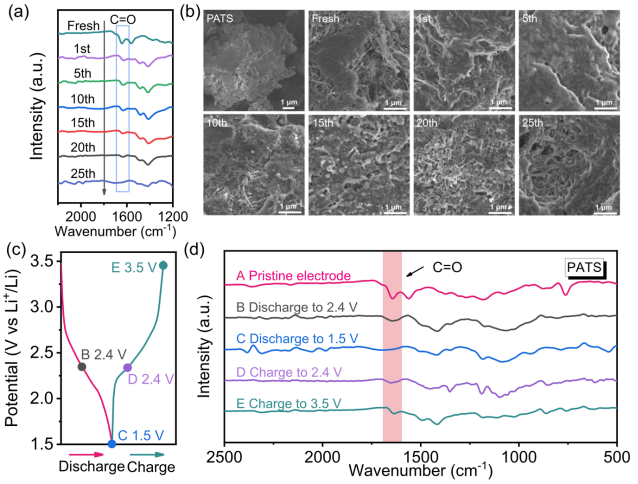

Figure 6. Mechanism investigation of the **PATS**-based battery. (a) Ex-situ FT-IR spectra of the **PATS** electrode recorded at the state (discharge to 1.5V) of different cycles, (b) ex-situ SEM images of **PATS** recorded at the powder, the fresh electrode, the state (discharged to 1.5 V) of the electrode for different cycles, (c) representative discharge and charge profiles of the **PATS** electrode, (d) ex-situ FT-IR spectra of the **PATS** electrode recorded at marked points **B-E** in (c).

Figure 5f shows the fitting of the linear relationship between Z' and $\omega^{-1/2}$; σ_w was calculated as 280.0, 172.3, 173.8, and 71.7 Ω $S^{-1/2}$ for **VO3**, **AT-Ph**, **PAT-Ph** and **PATS**, respectively. The smallest σ_w value (smallest slope of the linear trend) for **PATS** signifies faster ion-transport during electrochemistry. Accordingly, the Li^+ diffusion coefficients (D_{Li^+}) of the four electrodes were calculated according to equation 4:[59]

$$D_{Li^+} = \frac{R^2T^2}{2A^2n^4F^4C^2\sigma_w{}^2} \qquad (4)$$

where R is the gas constant, T is the absolute temperature of the test environment, A is the area of the electrodes, n is the number of electrons transferred, F is the Faraday constant, C is concentration of Li^+. As summarized in Table 1, the D_{Li^+} values of **PATS** were calculated to be 2.07×10^{-13} cm^2 s^{-1}, which is up to an order of magnitude higher than that of **VO3** (1.36×10^{-14} cm^2 s^{-1}), **AT-Ph** (3.60×10^{-14} cm^2 s^{-1}), and **AT-Ph** (3.53×10^{-14} cm^2 s^{-1}). Overall, the improvement of D_{Li^+} associated with the reduction of the R_{ct} implies faster ion- and electron-transport in the **PATS** electrodes, further corroborating its best performance in a battery setting.

In order to verify the Li^+ insertion and extraction process during charge and discharge, the reaction of **PATS** with lithium-based entities was further analyzed by ex-situ FT-IR spectroscopy. As shown in Figure 6a, the C=O peak weakens after the first discharge and completely disappears in the IR spectrum of the disassembled electrode after 25 discharges. This indicates **PATS** is completely lithiated into the discharge product after tens of cycles and is consistent with the "activation process" observed in the cycling test. During the first 25 cycles, insufficient contact between the polymer and the electrolyte leads to incomplete utilization of the C=O groups. The active materials of the internal bulk phase will only gradually be fully activated with increasing charge/discharge cycles. To verify this feature, the morphologies of the **PATS** electrode during cycling was investigated by SEM. As shown in Figure 6b, a fresh electrode clearly shows physical mixing of bulky **PATS** and MWCNTs, without intimate contact and even distribution. Under continuous cycling, a gel-like polymer film that evenly covers the MWCNTs is formed. Owing to the constant infiltration of the electrolyte, some pores start to appear on the electrode. Overall, as the electrode repeatedly swells and expels ions during charging and discharging cycles, more efficient conductive pathways would form, leading to the full activation of all C=O groups, and thus leading to an overall enhanced battery performance.

Moreover, the reversibility of the reduction process of **PATS** during charge/discharge was investigated. As presented in Figures 6c and 6d, when **PATS** is fully discharged to 1.5 V after activation, the characteristic IR peak for the C=O group at 1647 cm^{-1} disappears, suggesting that all carbonyl groups are consumed and converted to enolates along with Li^+ insertion. During charging, the peak gradually returns to the original state, validating its excellent reversibility. These results strongly confirm the reversible typical $2e^-$ reaction mechanism for anthanthrone species.

Full-Cell Battery Performance

To further evaluate the commercial application prospects of **PATS**, we subsequently assembled fully organic batteries that utilize **PATS** as cathode and graphite as anode. Figure 7a represents their schematic diagram. It should be noted that using 1 M $LiPF_6$ in EC/DMC/EMC (1:1:1, v/v/v) with 1 % VC as the electrolyte in the full-cell battery test ultimately led to a more stable performance (see the details in Figure S17). First, the electrochemical performance of **PATS** and graphite was evaluated in a half-cell configuration with Li-foil as the counter electrode. As shown in Figure 7b, the voltage plateaus in the half-cells are about 2.5 V and 0.2 V, respectively. The GCD curve of the **PATS** || graphite full cell exhibits an average working voltage of 2.3 V, corresponding to the difference in voltage plateaus between **PATS** electrode and the graphite electrode in half-cells. This result is consistent with the CV analysis that is shown in Figure 7c. The full-cell battery exhibits an excellent rate performance within a current density range of 0.1~1.0 A g^{-1} (Figure 7d). High capacities of 103, 92, 82, 74, 70, and 66 mAh g^{-1} can be obtained at current densities of 0.1, 0.2, 0.4, 0.6, 0.8, and 1.0 A g^{-1}. The fully organic battery delivers high energy density of 237 W h kg^{-1} with output voltage of 2.3 V, at a current density of 0.1 A g^{-1}. Furthermore, when the current density was reset to 0.1 A g^{-1}, the capacity returned to 101 mAh g^{-1}, indicating outstanding, recoverable rate capabilities.

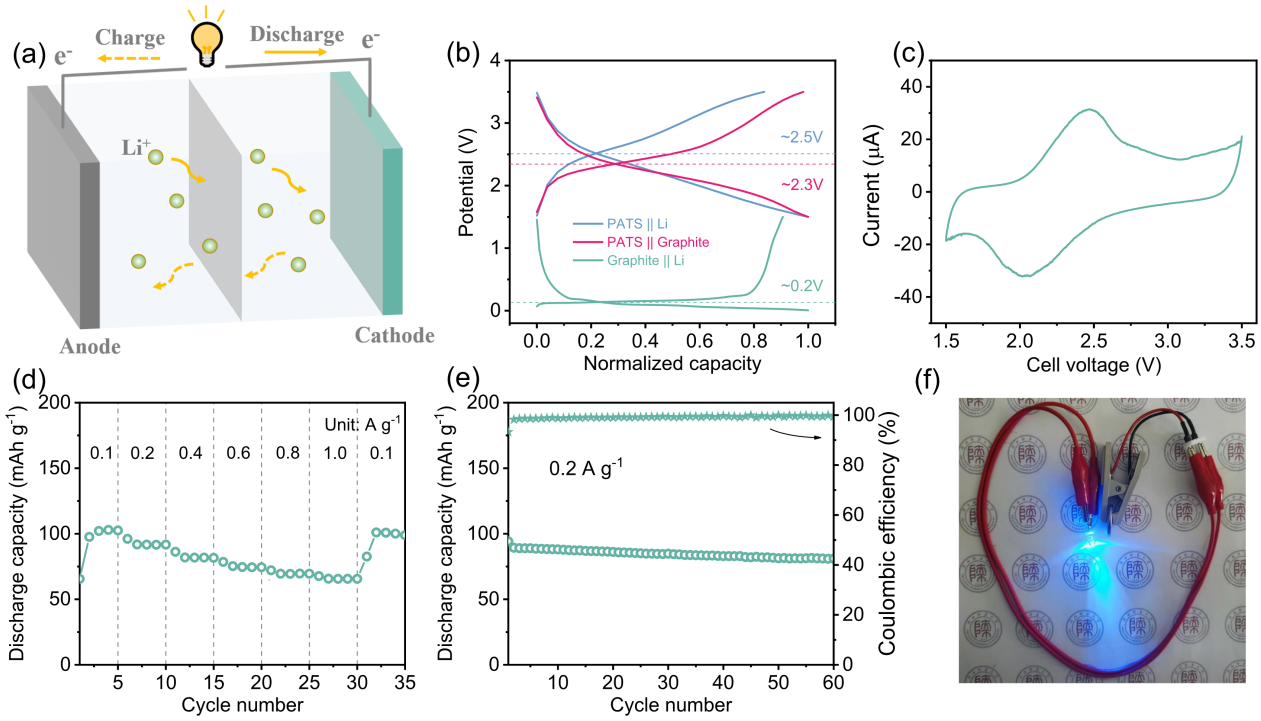

Figure 7. Performance of a fully organic battery based on a **PATS** cathode and a graphite anode. (a) Schematic diagram of the full battery, (b) normalized charge-discharge profiles of **PATS** || Li, graphite || Li and **PATS** || graphite, (c) CV of the fully organic battery at 0.2 mV s^{-1}, (d) rate performance at different current densities, (e) cycling performance at 0.2 A g^{-1}, (f) optical image demonstrating the full-cell device powering a blue LED.

The cycling performance of the ful-cell battery was further evaluated (Figure 7e), resulting in a capacity of 89 mAh g^{-1} at a current density of 0.2 A g^{-1} with a corresponding Coulombic efficiency of 99%. In addition, the cell maintains 91% capacity retention after 60 cycles, indicating an excellent long-term cyclability. Finally, one full-cell-based coin battery with **PATS** electrode can successfully light up a blue LED (shown in Figure 7f), demonstrating its potential for real-world applications.

Conclusion

With the aim of developing cost-effective organic cathodes for LOBs, we present the design of a class of anthanthrone-based species through simple and scalable synthesis from the cheap, commercially available two-electron acceptor **VO3**. The cyclability and rate performance are greatly improved when moving from small molecules to polymers, due to effectively suppressed dissolution of the active materials. In particular, **PATS** exhibits superb electrochemical performances in terms of high capacity, durability, rate performance, and redox kinetics, demonstrating its outstanding potential as cathode material. At a current density of 0.2 A g^{-1}, batteries that employ **PATS** as electrodes exhibited stable capacities up to 133 mAh g^{-1} after 300 cycles. The excellent electrochemical performance of **PATS** was found to be related to its higher lithium-ion diffusivity and smaller charge-transport resistance. Combined with its low cost, the impressive performance of **PATS** that is comparable to many other previously reported organic carbonyl species, makes it highly desirable as organic battery material (Table S2). Our results also demonstrate that thick (5.0 mg cm^{-2}) electrodes with a 60 wt % **PATS**, and high polymer-content electrodes (up to 80 wt %) exhibit decent battery performance. In addition, a fully organic battery using **PATS** as cathode and graphite as anode delivers an energy density of 237 Wh kg^{-1} with output voltage of 2.3 V, at a current density of 0.1 A g^{-1}. Overall, this work highlights that anthanthrone is a promising building block for incorporation into conjugated polymers for electrochemical energy-storage applications.

Experimental Section

Materials and Instruments

Polyvinylidene fluoride (PVDF) and 1-methyl-2-pyrrolidinone (NMP) were purchased from Shenzhen Kejing Zhida Technology Co., Ltd. LiTFSI, tetraethylene glycol dimethyl ether (G4), CR2032 battery cases, and separator (polypropylene, Celgard 2400) were purchased from DoDoChem. **VO3** was purchased from Alibaba and washed with H_2O and MeOH before use. All other chemical reagents were purchased from commercial sources (Aldrich, Alfa Aesar, Energy-chemical, Adamas) and were used as received, unless otherwise noted.

^{1}H NMR spectra were recorded on a JEOL JNM-ECZ400S/L1 NMR spectrometer. Solid-state ^{13}C NMR spectra were obtained on a JEOL JNM-ECZ400R/S1 NMR spectrometer at a MAS rate of 12 kHz. FT-IR spectra of power products were measured on a Bruker TENSOR27 spectrometer using a KBr pellet. FT-IR spectra of the electrode films were obtained on a PerkinElmer Frontier spectrometer. PXRD patterns were recorded on a Bruker D8 Advance instrument with Cu Kα X-ray radiation (λ = 1.5406 Å). TGA was conducted under a nitrogen atmosphere on a TA Q600 instrument with a heating rate of 10 °C min. XPS data was collected on a Shimadzu Axis UltraDLD instrument. UV-vis absorption spectra in solution were recorded on Cary 3500 spectrometer. The diffuse reflectance spectra of solid samples were recorded on a UV-Vis-NIR spectrophotometer (Lambda 1050) using $BaSO_4$ as the reference. SEM images were obtained using a Hitachi SU8220 system. Elemental analysis data were acquired on a Elementar Vario EL cube instrument. Theoretical

calculations have been carried out at the B3LYP/6-31G(d,p) level by using the GAUSSIAN 09 suite of programs.[60] The molecular electrostatic potential (MESP) was examined by using Multiwfn 3.8 and printed by VMD 1.9.3.[61-62]

Synthetic procedures

Synthesis of PATS. Under a nitrogen atmosphere, **VO3** (500 mg, 1.08 mmol, 1.0 eq.), $Na_2S \cdot 9H_2O$ (648 mg, 2.7 mmol, 2.5 eq.) and 10 mL of 1-methyl-2-pyrrolidinone (NMP) were added to a two-neck flask equipped with a condenser. The mixture was stirred for 30 min at room temperature and then heated at 205 °C for 16 h. After cooling to room temperature, 20 mL of H_2O and 10 mL of EtOH were added into the mixture under continuous stirring for 30 min. The mixture was then centrifuged and a black solid was collected. The solid powder was washed with H_2O, EtOH and acetone, respectively, several times. The product was dried at 60 °C in vacuum overnight, obtaining a black solid (Yield: 320 mg, 88 %).

Synthesis of AT-Ph. To a 100 mL two-necked round bottom flask equipped with a condenser, **VO3** (500 mg, 1.08 mmol, 1.0 eq.), phenylboronic acid (329 mg, 2.7 mmol, 2.5 eq.), $Pd(PPh_3)_4$ (62 mg, 0.054 mmol, 5 %), and 18-crown-6 (28 mg, 0.106 mmol, 10 %) were added. This mixture was put under three freeze-pump-thaw cycles before adding degassed mixture of toluene/EtOH (33 mL, 10:1, v/v), and aqueous K_2CO_3 (5 mL, 2 M) in sequence. The reaction mixture was then heated overnight under N_2 at 110 °C. After cooling to room temperature, the mixture was filtered and the solid was collected, further washed with water, EtOH and acetone. A yellow powder was obtained after vacuum oven drying (Yield: 430 mg, 87 %). ^{1}H NMR (400 MHz, $CDCl_3$): δ (ppm) = 8.81 (d, J = 6.8 Hz, 2H), 8.52 (s, 2H), 8.37 (d, J = 7.2 Hz, 2H), 7.84 (t, J = 7.6 Hz, 2H), 7.57 (m, 10H). Due to the limited solubility, no well-resolved ^{13}C NMR spectrum could be obtained.

Synthesis of PAT-Ph. The procedure was similar to that used to prepare **AT-Ph**, except 1,4-phenylenebisboronic acid (179 mg, 1.08 mmol, 1.0 eq.) was used in place of phenylboronic acid. The deep red solid was washed with H_2O, EtOH and acetone several times, and dried at 60 °C in vacuum overnight. (400 mg, 97 %).

Battery Fabrication and Testing

Half-Cell Fabrication. The working electrodes were prepared using NMP as solvent and mixing active material (**VO3** or **AT-Ph** or **PAT-Ph** or **PATS**), MWCNTs, and PVDF at a weight ratio of 6:3:1 (or 7:2:1 or 8:1:1 or 9:0:1 for the test of different content of conductive material). The electrodes were then prepared by casting the resulting inks onto aluminum foil via doctor blade. The fully prepared electrodes were dried at 80 °C for 12 h in a vacuum oven to remove any residual solvent. The electrodes were then cut into disks with a diameter of 12 mm. The mass loading of active material pasted on the aluminum foil was about 0.6 mg cm^{-2} (or 0.8~5.0 mg cm^{-2} for the test of different mass-loading). CR2032-type coin half-cells were assembled in an argon-filled glove box (< 0.1 ppm of oxygen, and < 0.01 ppm of water). Lithium foil (diameter = 16 mm) was employed as the counter electrode and a microporous polypropylene film (Celgard 2400) was applied as separator. 2.0 M LiTFSI in G4 (or 1 M $LiPF_6$ in EC/DMC/EMC (1:1:1, v/v/v) with 1 % VC) was used as the electrolyte. The batteries were left standing overnight before testing. The graphite electrodes were prepared by mixing the active materials with carbon black (ECP-600JD), and PVDF at a weight ratio of 8:1:1. The slurry was then casted onto copper foil for the electrochemical measurements. The typical average areal mass loading of graphite was about 1.5 mg cm^{-2}.

Full-Cell Fabrication. The prepared **PATS** electrodes were used directly without other handling. The prepared graphite electrodes were cycled 3 times and then discharged to 0.005 V to obtain the pre-lithiated graphite anode[63]. The fabrication process was similar to that of the half cells, except pre-lithiated graphite electrodes were used in place of lithium foil.

Test condition. Battery performance data were collected on a LAND CT2001A battery system at various current densities within a voltage window of 1.5–3.5 V at 30 °C. Cyclic voltammetry (CV) measurements of the batteries were performed on a CHI760 electrochemical workstation. The electrochemical impedance spectroscopy (EIS) was tested at a frequency range of 100 kHz to 0.1 Hz.

Acknowledgements

This work was supported by the Fundamental Research Funds for the Central Universities National (GK202201006) and the Innovation Capability Support Program of Shaanxi (No. 2020TD024). X. W. acknowledges the financial support from China Postdoctoral Science Foundation (No. 2020M683419). X. H. thanks Shaanxi Normal University for the funding support. T. B. thanks the Canada Research Chairs program for funding.

Keywords: anthanthrone • conjugated polymer • organic battery • polysulfide • vat orange 3

[1] M. Li, J. Lu, Z. Chen, K. Amine, *Adv. Mater.* **2018**, *30*, 1800561.
[2] M. Armand, J. M. Tarascon, *Nature* **2008**, *451*, 652-657.
[3] Z. Song, H. Zhou, *Energy Environ. Sci.* **2013**, *6*, 2280-2301.
[4] J. Kim, J. H. Kim, K. Ariga, *Joule* **2017**, *1*, 739-768.
[5] T. B. Schon, B. T. McAllister, P.-F. Li, D. S. Seferos, *Chem. Soc. Rev.* **2016**, *45*, 6345-6404.
[6] S. Lee, G. Kwon, K. Ku, K. Yoon, S.-K. Jung, H.-D. Lim, K. Kang, *Adv. Mater.* **2018**, *30*, 1704682.
[7] Y. Lu, J. Chen, *Nat. Rev. Chem.* **2020**, *4*, 127-142.
[8] K. Nakahara, S. Iwasa, M. Satoh, Y. Morioka, J. Iriyama, M. Suguro, E. Hasegawa, *Chem. Phys. Lett.* **2002**, *359*, 351-354.
[9] K. Zhang, Y. Hu, L. Wang, J. Fan, M. J. Monteiro, Z. Jia, *Polym. Chem.* **2017**, *8*, 1815-1823.
[10] K. Oyaizu, Y. Ando, H. Konishi, H. Nishide, *J. Am. Chem. Soc.* **2008**, *130*, 14459-14461.
[11] C. Karlsson, T. Suga, H. Nishide, *ACS Appl. Mater. Interfaces* **2017**, *9*, 10692-10698.
[12] M. Kolek, F. Otteny, P. Schmidt, C. Mück-Lichtenfeld, C. Einholz, J. Becking, E. Schleicher, M. Winter, P. Bieker, B. Esser, *Energy Environ. Sci.* **2017**, *10*, 2334-2341.
[13] F. Otteny, G. Studer, M. Kolek, P. Bieker, M. Winter, B. Esser, *ChemSusChem* **2020**, *13*, 2232-2238.
[14] P. Acker, L. Rzesny, C. F. N. Marchiori, C. M. Araujo, B. Esser, *Adv. Funct. Mater.* **2019**, *29*, 1906436.
[15] J. A. Kowalski, M. D. Casselman, A. P. Kaur, J. D. Milshtein, C. F. Elliott, S. Modekrutti, N. H. Attanayake, N. Zhang, S. R. Parkin, C. Risko, F. R. Brushett, S. A. Odom, *J. Mater. Chem. A* **2017**, *5*, 24371-24379.
[16] B. Wei, Y. Hong, W. Tang, M. Guo, X. He, C. Tang, J. Hu, C. Fan, *Chem. Eng. J.* **2023**, *451*, 138773.
[17] S. Xu, H. Dai, S. Zhu, Y. Wu, M. Sun, Y. Chen, K. Fan, C. Zhang, C. Wang, W. Hu, *eScience* **2021**, *1*, 60-68.
[18] L. Chen, C. R. Bridges, G. Gao, T. Baumgartner, X. He, *ACS Appl. Energy Mater.* **2019**, *2*, 7315-7320.
[19] K. Oka, R. Kato, K. Oyaizu, H. Nishide, *Adv. Funct. Mater.* **2018**, *28*, 1805858.
[20] C. Luo, O. Borodin, X. Ji, S. Hou, K. J. Gaskell, X. Fan, J. Chen, T. Deng, R. Wang, J. Jiang, C. Wang, *Proc. Natl. Acad. Sci. USA* **2018**, *115*, 2004-2009.
[21] C. Luo, X. Ji, S. Hou, N. Eidson, X. Fan, Y. Liang, T. Deng, J. Jiang, C. Wang, *Adv. Mater.* **2018**, *30*, 1706498.
[22] M. Stolar, C. Reus, T. Baumgartner, *Adv. Energy Mater.* **2016**, *6*, 1600944.
[23] G. Li, B. Zhang, J. Wang, H. Zhao, W. Ma, L. Xu, W. Zhang, K. Zhou, Y. Du, G. He, *Angew. Chem. Int. Ed.* **2019**, *58*, 8468-8473.
[24] T. Ma, L. Liu, J. Wang, Y. Lu, J. Chen, *Angew. Chem. Int. Ed.* **2020**, *59*, 11533-11539.

[25] L. Chen, X. Zhu, Y. Zhang, G. Gao, W. Xue, S. Zhang, X. Wang, Q. Zhang, X. He, *J. Mater. Chem. A* **2021**, *9*, 18506-18514.
[26] A. Jouhara, E. Quarez, F. Dolhem, M. Armand, N. Dupré, P. Poizot, *Angew. Chem. Int. Ed.* **2019**, *58*, 15680-15684.
[27] T. B. Schon, A. J. Tilley, C. R. Bridges, M. B. Miltenburg, D. S. Seferos, *Adv. Funct. Mater.* **2016**, *26*, 6896-6903.
[28] G. Gao, X. Wang, L. Chen, T. Baumgartner, X. He, *Chem. Mater.* **2021**, *33*, 4596-4605.
[29] X. Wang, W. Xue, G. Gao, L. Chen, T. Baumgartner, X. He, *Cell Rep. Phys. Sci.* **2022**, *3*, DOI: 10.1016/j.xcrp.2022.100951.
[30] L. Zhu, G. Ding, L. Xie, X. Cao, J. Liu, X. Lei, J. Ma, *Chem. Mater.* **2019**, *31*, 8582-8612.
[31] S. Cao, H. Zhang, Y. Zhao, Y. Zhao, *eScience* **2021**, *1*, 28-43.
[32] D. L. Williams, J. J. Byrne, J. S. Driscoll, *J. Electrochem. Soc.* **1969**, *116*, 2.
[33] Y. Lu, X. Hou, L. Miao, L. Li, R. Shi, L. Liu, J. Chen, *Angew. Chem. Int. Ed.* **2019**, *58*, 7020-7024.
[34] W. Huang, Z. Zhu, L. Wang, S. Wang, H. Li, Z. Tao, J. Shi, L. Guan, J. Chen, *Angew. Chem. Int. Ed.* **2013**, *52*, 9162-9166.
[35] J. Yang, P. Xiong, Y. Shi, P. Sun, Z. Wang, Z. Chen, Y. Xu, *Adv. Funct. Mater.* **2020**, *30*, 1909597.
[36] W. Huang, S. Liu, C. Li, Y. Lin, P. Hu, Z. Sun, Q. Zhang, *EcoMat.* **2022**, *4*, e12214.
[37] S. Cao, H. Zhang, Y. Zhao, Y. Zhao, *eScience* **2021**, *1*, 28-43.
[38] Y. Hong, J. Hu, W. Tang, B. Wei, M. Guo, S. Jia, C. Fan, *Energy Storage Mater.* **2022**, *52*, 61-68.
[39] W. Zhang, H. Tian, J. Wang, H. Sun, J. Wang, W. Huang, *ACS Appl. Mater. Interfaces* **2022**, *14*, 38887-38894.
[40] J. Zhang, Z. Song, L. Zhan, J. Tang, H. Zhan, Y. Zhou, C. Zhan, *J. Power Sources* **2009**, *186*, 496-499.
[41] X. Han, C. Chang, L. Yuan, T. Sun, J. Sun, *Adv. Mater.* **2007**, *19*, 1616-1621.
[42] Z. Song, H. Zhan, Y. Zhou, *Chem. Commun.* **2009**, 448-450.
[43] Y. Hu, Y. Gao, L. Fan, Y. Zhang, B. Wang, Z. Qin, J. Zhou, B. Lu, *Adv. Energy Mater.* **2020**, *10*, 2002780.
[44] K. Liu, J. Zheng, G. Zhong, Y. Yang, *J. Mater. Chem.* **2011**, *21*, 4125-4131.
[45] T. Sun, Z.-J. Li, Y.-F. Zhi, Y.-J. Huang, H. J. Fan, Q. Zhang, *Adv. Funct. Mater.* **2021**, *31*, 2010049.
[46] Z. Song, Y. Qian, M. L. Gordin, D. Tang, T. Xu, M. Otani, H. Zhan, H. Zhou, D. Wang, *Angew. Chem. Int. Ed.* **2015**, *54*, 13947-13951.
[47] W. Choi, D. Harada, K. Oyaizu, H. Nishide, *J. Am. Chem. Soc.* **2011**, *133*, 19839-19843.
[48] J.-B. Giguère, Q. Verolet, J.-F. Morin, *Chem. Eur. J.* **2013**, *19*, 372-381.
[49] J. T. J. Edmonds, H. W. J. Hill, *US Pat.* **1963**, 3354129.
[50] B. K. Shah, D. C. Neckers, J. Shi, E. W. Forsythe, D. Morton, *J. Phys. Chem. A* **2005**, *109*, 7677-7681.
[51] P. Ribar, L. Valenta, T. Šolomek, M. Juríček, *Angew. Chem. Int. Ed.* **2021**, *60*, 13521-13528.
[52] H.-g. Wang, Q. Li, Q. Wu, Z. Si, X. Lv, X. Liang, H. Wang, L. Sun, W. Shi, S. Song, *Adv. Energy Mater.* **2021**, *11*, 2100381.
[53] J. Wang, J. Polleux, J. Lim, B. Dunn, *J. Phys. Chem. C* **2007**, *111*, 14925-14931.
[54] V. Augustyn, J. Come, M. A. Lowe, J. W. Kim, P.-L. Taberna, S. H. Tolbert, H. D. Abruña, P. Simon, B. Dunn, *Nat. Mater.* **2013**, *12*, 518-522.
[55] H. Gao, A. R. Neale, Q. Zhu, M. Bahri, X. Wang, H. Yang, Y. Xu, R. Clowes, N. D. Browning, M. A. Little, L. J. Hardwick, A. I. Cooper, *J. Am. Chem. Soc.* **2022**, *144*, 9434-9442.
[56] T. C. Liu, W. G. Pell, B. E. Conway, S. L. Roberson, *J. Electrochem. Soc.* **1998**, *145*, 1882-1888.
[57] G. Wang, N. Chandrasekhar, B. P. Biswal, D. Becker, S. Paasch, E. Brunner, M. Addicoat, M. Yu, R. Berger, X. Feng, *Adv. Mater.* **2019**, *31*, 1901478.
[58] J. Wang, H. Liu, C. Du, X. Zhang, Y. Liu, H. Yao, Z. Sun, S. Guan, *Chem. Eng. J.* **2022**, *444*, 136598.
[59] Y. Cui, X. Zhao, R. Guo, *Electrochim. Acta* **2010**, *55*, 922-926.
[60] M. J. Frisch, et al, **2010**, Gaussian 09, Revision B.01 (*Gaussian, Inc, Wallingford CT*).
[61] T. Lu, F. Chen, *J. Comput. Chem.* **2012**, *33*, 580-592.
[62] W. Humphrey, A. Dalke, K. Schulten, *J. Molec. Graphics* **1996**, *14*, 33-38.
[63] K. Zou, W. Deng, P. Cai, X. Deng, B. Wang, C. Liu, J. Li, H. Hou, G. Zou, X. Ji, *Adv. Funct. Mater.* **2021**, *31*, 2005581.

Entry for the Table of Contents

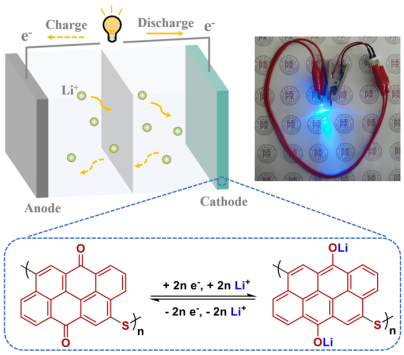

A new class of anthanthrone-based organics with excellent performance and stability in secondary batteries can easily be prepared through simple and scalable synthesis from the very cheap, commercially available dye vat orange 3 (**VO3**). This work highlights that anthanthrone is a promising building block in conjugated polymers for energy-storage applications.